Shape optimization for the noise induced by the flow over compact bluff bodies

Wagner José Gonçalves da Silva Pinto, Florent Margnat

Shape optimization for the noise induced by the flow over compact bluff bodies

Wagner José Gonçalves da Silva Pinto, Florent Margnat[1]

Institut PPRIME, Department of Fluid Flow, Heat Transfer and Combustion, Université de Poitiers - ENSMA - CNRS, Building B17 - 6 rue Marcel Doré - TSA 41105 86073, POITIERS CEDEX 9, France

Abstract

A shape optimization for tonal noise generated aerodynamically at low Mach number is performed for a cylinder with polygonal cross-section. Acoustic quantities are derived from a hybrid analytical formula, with aeroacoustic sources obtained from the incompressible solution of the direct Navier-Stokes equations in 2D at Re = 150; the solid domain is modelled by an Immersed Boundary Method. The optimization is done with the Particle Swarm Optimization (PSO) technique and performed in a cluster where each cost function evaluation is an independent flow simulation. The precision on the 4 main shape parameters is set to 0.001, consistently with the convergence criteria in time, grid and swarm. Optimal shapes for minimum drag and minimum acoustic power are relatively similar. A large range between the optimal shapes is obtained: factor 1.8 for drag and 20 dB for the acoustic power. The reduction of noise is associated with long and bluffer geometries, while the louder flows are associated with highly interacting shear layers obtained with back pointing triangles. The fluctuating lift is the major quantity to control noise at fixed length, while increasing the aspect ratio tends to reduce the noise for globally all geometries. An overall correlation between mean drag and fluctuating suction is also noticed.

Keywords: aeroacoustics, bluff-body noise, shape optimization, Particle Swarm Optimization, Immersed Boundary Method

1. Introduction

1.1. The influence of shape on body noise

The overall goal of the present study is the understanding of bluff body noise, in particular the influence of shape. This mostly concerns sources of acoustical discomfort that salient parts of vehicles can be, for instance car antenna and rear mirrors, high-speed train pantographs and landing gears. Such engineering cases still faces a lack of models which could be used for low-cost diagnostics [1] at the design step. Indeed, to date, there is no aeroacoustic equivalent of head loss tables or Nusselt's number formulas to apply to

[1]Corresponding author: florent.margnat@univ-poitiers.fr

typical configurations. This may be attributed to our incomplete understanding of the link between the body shape and noise.

The problem of noise generation by fluid flow including boundary has been fully put in equations by Ffowcs-Williams and Hawkings [2], who extended to moving surfaces Curle's solution [3] of Lighthill's theory [4] for fixed surfaces. Alternative views are brought by the theory of vortex sound [5, 6] and of acoustic diffraction [7, 8, 9]. These sets of equations can often be numerically solved at lower costs than the full compressible Navier-Stokes equations. However, these acoustic analogies still require input of the unsteady flow field to build the source terms, thus this are hardly exploitable as a design tool. Nevertheless, through dimensional analysis, these theoretical works has yielded the fruitful practical message that, at low Mach number, noise intensity scales with the flow velocity with a high power: fifth for diffraction driven cases [7, 10] to eight for boundary layer [11, 12] or free shear flow [13, 14].

Indeed, considering the case of a long cylinder, Curle [3] estimated that the total acoustic power output should be roughly proportional to $\rho_0 U_\infty^6 \delta^2 / c_0^3$ *times a function of the Reynolds number* (Re), where δ is *a typical dimension of the solid body* (the other symbols are intuitive and explicitely defined in Section 2.1). A few months later, Phillips [15] correlated an analytical expression of the lift force fluctuation on the circular cylinder with experimental data. He then stated that the total radiated intensity should be about $\kappa \sin^2\theta \ \rho_0 U_\infty^6 \ \mathrm{St}^2 \ ld/(c_0^3 R^2)$, where d is the diameter and l is the length of the cylinder. The numerical constant κ depends on the Reynolds number through the length scale Λ of the fluctuations of lift along the cylinder axis. For $100 < \mathrm{Re} < 160$, he reported $\kappa \approx 0.27$, while at higher Re when the cylinder wake becomes turbulent, the value is reduced to $\kappa \approx 0.037$ for the range $360 < \mathrm{Re} < 30000$. Similarly, Howe [16] derived an expression for the acoustic intensity that does not depend explicitly on the diameter but on the product $l\Lambda$, arguing that Λ itself may be about $3d$ for $\mathrm{Re} > 300$. A sound pressure coefficient was also defined by Keefe [17] as $\overline{C_L'^2}\mathrm{St}\sqrt{\Lambda/d}$. Thus, a general conclusion is that acoustic radiation is quantified by the energy supplied in the force fluctuation, weighted by the axial length over which that energy behaves as an efficient radiator, both parameters being dependant on the Reynolds number. However, models for the unsteady flow properties (force fluctuation and its spanwise correlation scale) still relay highly in empiricism [18], and are focused mainly on circular and square cylinders. Qualitative and quantitative descriptions of the influence of the shape in the wake structure are sparse.

Recently, an expression of the acoustic power has been derived [19] from Curle's formula for a compact body, considering the 2D case and a tonal emission. It includes both lift and drag levels of fluctuations, and no arbitrary choice of typical length. Thus, being an analytical formula, it reduces the numerical setup and cost to that necessary for the hydrodynamic flow, and allows the specific study and modelling of the shape influence on noise. In the present paper, this is done through shape optimization, thinking that the exhibition of extreme behavior may facilitate the eduction of the driving mechanisms.

1.2. Shape optimization for aeroacoustics

Apart of classical derivative based optimizers, meta-heuristic techniques work with the objective function being a black box. No previous knowledge of the behavior of the function or the response surface is needed to achieve a converging point, only the evaluation of point-wise calculations. The most interesting aspect of this kind of optimizer is the capability to be set to find global extrema and in general, easy implementation and parallel evaluation. Most of those optimizers are a reproduction of a natural phenomenon, such as the Darwin's theory of biological evolution (for example, Genetic Algorithms [20] - GA and Differential Evolution [21] - DE) and the social behavior of animals (Ant Colony Optimization [22] - ACO and Particle Swarm Optimization [23] - PSO). Recent uses of this family of optimizers in the field of aerodynamics addressed the shape optimization of high-speed trains [24]; the optimization of wings [25]; the aerodynamic and aeroacoustic optimization of an extended Ahmed body [26]; the high speed train nose optimization [27], and the multi-objective PSO study of the noise emission of circular cylinders with a splitter plate [28].

Here, the robust meta-heuristic optimization routine based on swarm intelligence, Particle Swarm optimization (PSO), is implemented. The hybrid evaluation of the noise production is assessed by the above mentionned analytical formula [19] which needs a complete flow evaluation. Current approach uses direct Navier-Stokes (DNS) calculation, for the precision of the technique and its realistic detachment prediction. This leads to impose a low Reynolds number regime. However, in many experiments [29, 30, 31, 32], the frequency associated with lift fluctuations remains the principal peak of the noise spectra at high Reynolds number even if the Strouhal number can undergo a slight increase. Thus, a low Reynolds number regime is relevant not only for the study of the wake dynamics close to the onset of unsteadiness, but for a greater range of flows. It also greatly reduces the computational cost of the study, allowing it to be conducted in 2D. This naturally misses one major ingredient of cylinder aeroacoustics that is the source spanwise decorrelation. However, the sectional behavior is of interest by itself and the shape influence on it may be even more major [32]. Finally, an Immersed Boundary Method (IBM) is used for modelling the no-slip condition, thus allowing the simulation of thousands of shapes with a single, qualified grid.

The global optimization procedure thus combines PSO with an analytical formula which directly estimates the acoustic power from aerodynamic quantities obtained from DNS embedding IBM. It was described in details in [33]. The present study is focused on enlarging the range of the outputs by introducing a new parameterization of the shape, which is here based on four vertex connected with straight segments and freely moving on the sides of a rectangle. Moreover, a careful description is included of what the settings are so that global precision is coherent and leads to relatively robust optimizations in spite of errors and uncertainties at each stage (e. g. grid refinement, optimization convergence, etc.).

The paper is organized as follows. Section 2 contains the description of the solver (2.1), the numerical setup and the mesh and domain independence studies (2.2). In Section 3, the optimization technique and the geometry parametrization are detailed. The results of the application of the optimization procedures for

optimal drag and noise power are assembled in Section 4, with a discussion of the obtained flow and integral quantities as well as the discrimination between the geometrical features that influences vortex shedding and sound emission. Some concluding remarks finalize the document in Section 5.

2. Aeroacoustic methodology and qualification

2.1. Acoustic power estimation

An aeroacoustic analogy is used in this study. The hybrid solution provides a criterion for the optimization, on this case, the acoustic power W of the tonal noise emission by the flow over a body is selected. It is deduced from Curle's solution for an acoustically compact body in 2D by [19]:

$$W = \frac{\pi}{16} d \rho_0 U_\infty^3 \ \mathrm{M}^2 \ \mathrm{St} (2 {C'_D}^2 + {C'_L}^2) \tag{1}$$

where W is the acoustic power (integral of the acoustic intensity over any observer circle in the far-field), ρ_0 is the density in the propagation medium, U_∞ is the upstream velocity, d is the main cross section. The Strouhal number St is based on U_∞, d, and the main frequency of lift fluctuations. Noting c_0 the sound velocity, the Mach number is $\mathrm{M} = U_\infty / c_0$. C'_D and C'_L are the period's root mean square (RMS) of the fluctuations of the drag (F_1) and lift (F_2) coefficients, defined per unit length of cylinder:

$$C_D = \frac{F_1}{\frac{1}{2} \rho_0 U_\infty^2 d} \qquad C_L = \frac{F_2}{\frac{1}{2} \rho_0 U_\infty^2 d} \tag{2}$$

Formula (1) is a long-wavelength approximation, but it is not the result of a dimensional analysis since this would need that typical scales of lengths and velocity have been estimated, like for the U^6 law. Reference length and velocity are involved here only for the definition of the Mach and Strouhal numbers and of the aerodynamic force coefficients. Moreover, involving C'_L and C'_D, (1) does account for the shape dependence, which Curle's U^6 law misses.

The flow is numerically predicted by direct solution of the incompressible Navier-Stokes equations (DNS) using *incompact3d* [34]. This solver uses a 6th order centered finite differences scheme in space (degraded on borders) and 3rd order explicit Runge-Kutta scheme in time. The incompressible assumption for the evaluation of the aeroacoustic source quantities is supported by the fact that in the case of a compact surface, the net force on the body is almost always dominated by purely hydrodynamic effects [8]. Moreover, it has been numerically assessed for free [35] and body [19] flows by comparison with direct noise computations, at Mach numbers around 0.3.

The solid domain is modelled by an Immersed Boundary Method (IBM) [36] where a forcing term $\mathbf{f}$ is added to the momentum equation:

$$\frac{\partial \mathbf{u}_i}{\partial t} + \mathbf{u}_j \frac{\partial \mathbf{u}_i}{\partial y_j} = -\frac{\partial}{\partial y_j}[p\delta_{ij} - \tau_{ij}] + \mathbf{f}_i \qquad \text{with} \qquad \mathbf{f}(\mathbf{y},t) = -\epsilon(\mathbf{y}) \left[\omega_n^2 \int_0^t \mathbf{u}(\mathbf{y},t)dt + 2\zeta\omega_n \mathbf{u}(\mathbf{y},t)\right] \quad (3)$$

where $\omega_n = 50$ and $\zeta = 1$, values selected from [37], are the natural frequency and the damping coefficient, respectively, of the second order controller that forces a null velocity everywhere ϵ is non zero. No interpolation correction is used to refine the geometry description. A remarkable advantage of this approach is that the integration of the forcing terms over the solid domain gives directly the resulting aerodynamic forces acting on the obstacle, that is, C_D and C_L. Any arbitrary solid shape is modelled with the modification of the ϵ matrix in the same Cartesian grid, an extremely advantageous asset for the use of this technique in optimization, where hundreds to thousands of geometries must be studied.

2.2. Numerical Setup and Validation

The present analysis is performed with Reynolds number $Re = U_\infty d/\nu$ of 150, where ν is the kinematic viscosity. The small Reynolds number is mandatory so the physics of the problem can be reproduced in a 2D simulation, however, for the wide range of geometries that are considered in the optimization, there are no warranties that the flow is always well described without the third dimension. For this regime, both drag and lift are close to sinusoidal signals, so the flow periods are defined from consecutive lift peaks. The final simulated period statistics (C_D, C_L and St) are used for the analysis presented on this paper. In order to compute (1), the Mach number is arbitrarily set to 0.1, without any consequence on the comparisons between shapes in the same conditions.

Uniform velocity is set inflow, while a convection condition is set outflow; lateral boundaries are defined with free slip condition. Mesh is uniform in flow direction and stretched in transverse direction, with grid points concentrated in the center, see [34]. Flow initial condition is uniform and equals inlet velocity, $u_1 = U_\infty$ and $u_2 = 0$, for the complete domain including the solid elements. No disturbance is added, once the transient from the IBM elements are sufficient to give onset to the flow periodicity. A scheme of the domain is presented in Figure 1. Lateral boundaries are fixed at $20d$ for a blockage ratio of 5%, based on [38].

Domain and mesh independence tests are performed for both upstream and downstream distances of the vertical boundaries (X^u and X^d, respectively) and element size (number of grid elements). Not only to quantify the consistency of the numerical setup, this study is also aimed to reduce both memory and time requirements for the use of the DNS simulations for a stochastic optimization that requires the evaluation of thousands of cases, while correctly representing the physics of the problem.

The tests are performed with an arbitrary symmetrical shape of height d and length $2d$, composed by half ellipse at the leading edge ($y_1 \leq -0.1L$) and two second degree polynomials on trailing edge, enabling C^1 and C^2 continuities with the ellipse. The solid domain is the set of grid points that are inside the selected

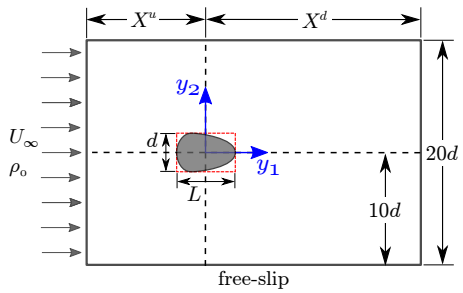

Figure 1: Scheme of numerical domain with the shape used in the convergence studies.

closed contour, defined by ones on the $\epsilon(\mathbf{y})$ matrix. The use of a non-canonical geometry for this step is justified by the intended use of its conclusions, once there is no restriction of the geometry that is going to be observed when running the optimization.

2.2.1. Domain convergence

The domains analysis is performed for different streamwise extensions, with a variable number of grid points to maintain the elements' size constant. The number of mesh points in both transverse and flow direction is chosen as a multiple of small prime factors + 1 for a better performance of the spectral solution of the Poisson equation, consequently, they are the parameters that defined the selected test distances. Mesh elements are of size $(\Delta y_1, \Delta y_2) = (1.953, 1.125) \times d/100$ at $y_2 = 0$, and timestep duration is of $\Delta t = 0.0042 d/U_\infty$, with a Courant number of CFL $= 0.21$; calculation stops at 40,000 timesteps ($t = 170 \times d/U_\infty$).

Simulations are performed for asynchronous variations of X^u and X^d, being the complementary distance fixed at an arbitrary level issued from previous testing. These evaluations are based on the hypothesis that the effect of the modification of a boundary location is independent of the position of the other for the chosen complementaries ($X^u = 12d$ and $X^d = 18d$). Results are presented on Figure 2 for the variables of interest (mean drag $|C_D|$ and fluctuating lift C'_L). Other aerodynamic quantities present in the aeroacoustical model are also analysed, but not graphically presented here for compactness.

Asymptotic curves are obtained for both X^u and X^d, similarly to the results for circular section by Posdziech and Grundmann [39]. Simultaneously, it is observed that an increase in those two reduces the levels of fluctuating lift and drag. The order is not similar for mean drag and Strouhal number: they are monotonically increasing for X^u and monotonically decreasing for X^d. According to this tendency, variations of the actual boundaries distances from the section edges caused by the modifications of the length of the geometries in the optimization procedures are always advantageous, once they are smaller than the value used in the convergence tests ($L \leq 2d$).

Inflow distance has more influence in the flow response due to the modification of upstream conditions in the presence of the obstacle, even at large X^u. The obtained curves confirm that the selected fixed value

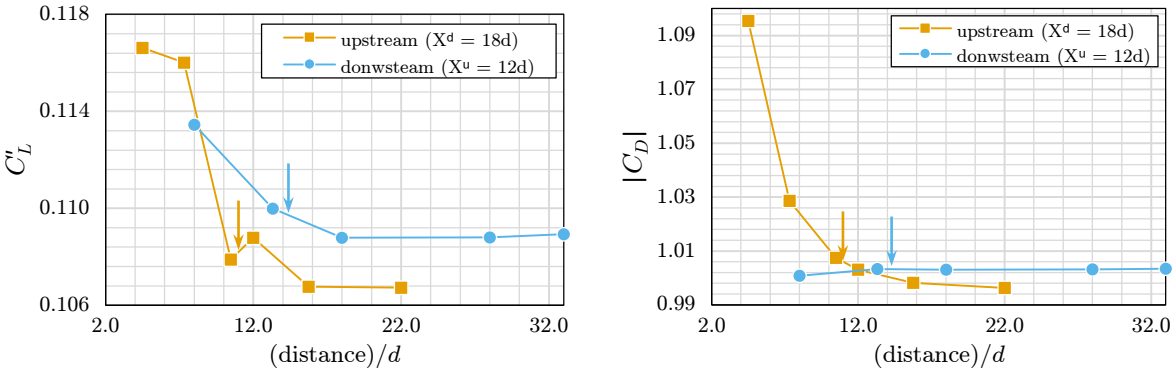

Figure 2: Influence of domain upstream and downstream distances on fluctuating lift and mean drag. Arrows point to the selected configurations.

for the complementary distance are coherent in terms of flow physics.

For a precision of about 1%, the selected values for the final domain are $X^u = 11d$ and $X^d = 14.31d$, what represents a mesh of 1297×513 grid points. Simulations are performed for the selected domain and the final result is compared to the extrema of the domain study, as presented on Table 1.

Table 1: Aerodynamic quantities' errors between the final domain and the most extended boundaries.

case	X^u/d	X^d/d	$\Delta\lvert C_D\rvert$	$\Delta C'_L$	$\Delta C'_D$	ΔSt
X^u max	22.0	18.0	-3.2%	-1.2%	-13.5%	-0.8%
X^d max	12.0	33.0	-1.1%	-0.5%	-10.4%	-0.4%

Final domain has higher level for all quantities, as indicated on Figure 2, albeit the discrepancies are relatively small. The fluctuating drag has an elevated offset (order of 10%) provoked by its low order O(-4) and thus has an insignificant influence in the aeroacoustical result. Once the domain is defined, further steps are performed for reducing the calculation time.

2.2.2. Mesh convergence

When comparing the element size, the ratio between number of elements in streamwise and spanwise directions is maintained, thus, the elements are isotropically contracted or expanded. A total of 5 meshes are tested, being number 4 the mesh used on the domain study and number 5 the most refined. The timestep physical duration is modified to guarantee numerical convergence, and the number of timesteps is chosen to achieve at least $225 \times d/U_\infty$ of physical time, within which the comparisons are performed. Evolution of the size of the elements is presented in Table 2, with the normalized element size and the number of elements per d, and Figure 3 presents the results for fluctuating lift and mean drag.

Table 2: Mesh size.

mesh	1	2	3	4	5
$(\Delta y_1/d)$	0.052	0.039	0.026	0.020	0.013
$(\Delta y_1/d)^{-1}$	19.2	25.6	38.4	51.2	76.8
$(\Delta y_2/d)_{min}$	0.030	0.023	0.015	0.011	0.008
$(\Delta y_2/d)^{-1}_{min}$	33.3	44.4	66.6	88.9	133.3

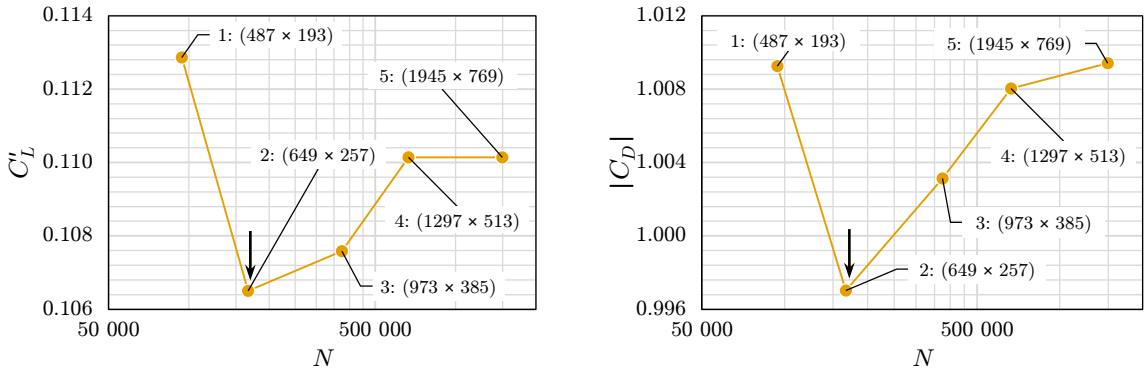

Figure 3: Influence of mesh refinement in fluctuating lift and mean drag. Tags indicate the number of elements in flow and transverse directions, respectively, and arrows point to the selected configuration.

For the presented quantities, there is a maximum offset of 1.2% for C'_L and 3.3% for $|C_D|$, when compared to the most refined grid. There is a 8.5% deviation for C'_D and 0.4% for the Strouhal number. The small impact of the mesh refinement can be associated to the flow regime, because once the Reynolds number is small, the flow presents very large boundary layers that are less influenced by small oscillations in the solid elements size and position. Observed fluctuations may be associated with the modifications of the dynamic of the solid domain by the consistent change in the number of solid points, once the finite difference scheme is unchanged and there are no interpolations on the obstacle wall.

Following the behaviour of the global coefficients, a similarly good result is also obtained when spanwise velocity profiles are compared, as showed in figure 3. The mean and RMS velocity profiles at $y_1 = 0$ of the last 2 simulated periods are presented for meshes 2 and 5.

Profile comparisons at upstream ($y_1 = -5d$) and downstream ($y_1 = +5d$ and $y_1 = +10d$) positions are performed similarly to the analysis executed at the central spanwise axis ($y_1 = 0$). Considering all 4 profiles, there are a maximum deviation of 1% for the mean velocity and of $8 \times 10^{-3} \times U_\infty$ for RMS velocity profiles.

In a search for a compromise between time consumption and physical representativeness, mesh number 2 is selected. For the chosen space discretisation, there are about 25 elements by diameter in y_1 and 50 in

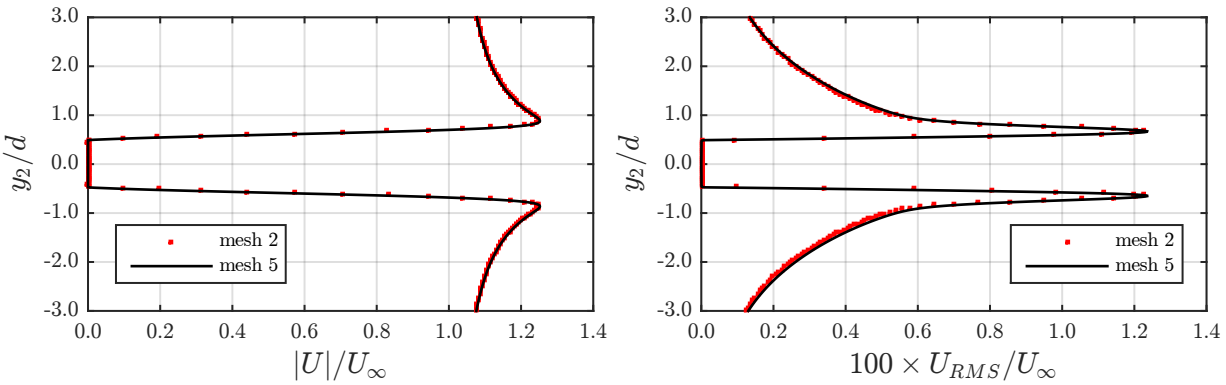

Figure 4: Influence of mesh refinement in mean (left) and RMS (rigth) velocity profiles at $y_1 = 0$.

y_2. There is a slight loss in accuracy, however, for an equal flow time and CPU conditions, calculation time is reduced to 2.5% of the one obtained with mesh number 5. For 50,000 timesteps, an average CPU time of 2 hours is needed for a single simulation.

Though similar accuracy could be obtained with even coarser meshes, the corresponding geometrical precision would be reduced leading to the fact that relatively large modifications of parameters would be irrelevant for the solver. The consistency of the optimization depends on the fact that variations of the theoretical geometry are well represented in the solver, even if the difference in the aeroacoustic answer is not significant, respecting the physics of the cost function.

2.2.3. Time convergence

Once the domain and the mesh are fixed, further analysis must be performed to check in time convergence. Figure 5 illustrates drag evolution and the convergence of the period aerodynamic quantities, based on the relative error of the 10 points moving average. A convergence of 0.01% is observed for the quantities of interest at $t = 300 \times d/U_\infty$. The Strouhal number (not shown) does not oscillate after $t = 150 \times d/U_\infty$, what can be explained by the limits in the technique used for determining it (inverse of a lift period, maximum precision being the duration of a timestep).

Convergence in time is also regarded for the different meshing configurations from the previous studies. Apart from differences in time required for the settlement of the periodic wake structure, as noted on Figure 5, there is no significant variation of convergence errors or convergence time as a function of either the domain size or the discretization level.

2.2.4. Validation

Based on mesh and domain independence studies, final mesh ($X^u, X^d = 11d, 14.31d$ and a grid of 649×257 points) is used for a validation procedure against literature values for 40,000 timesteps ($t = 288 \times d/U_\infty$). Simulations are performed with canonical geometries at different lengths and Reynolds

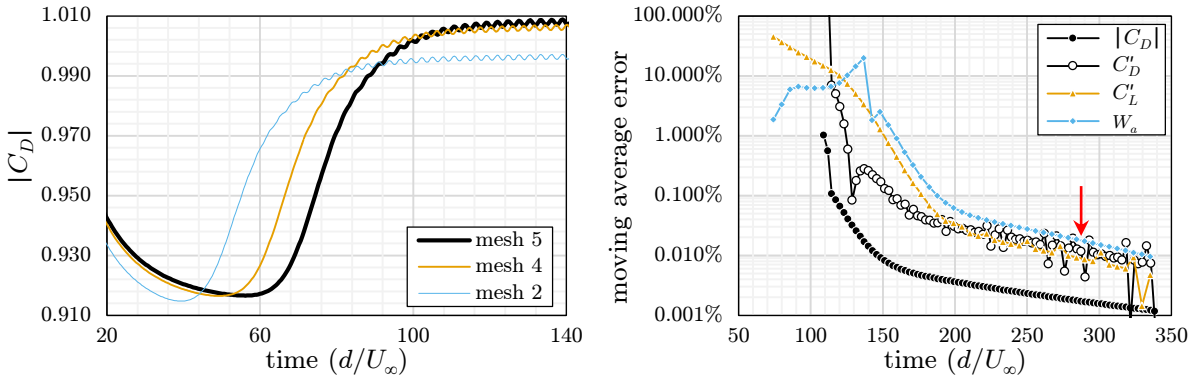

Figure 5: Time evolution of drag coefficient for different meshes (left) and time convergence of mean drag, fluctuating drag and lift and acoustic power for the final domain, with mesh 4 (right). Arrow points to the selected simulation duration.

numbers. The mean drag of a circular cylinder and RMS lift of rectangular cylinders are compared with literature values [40, 39, 41, 42] and presented in Figure 6.

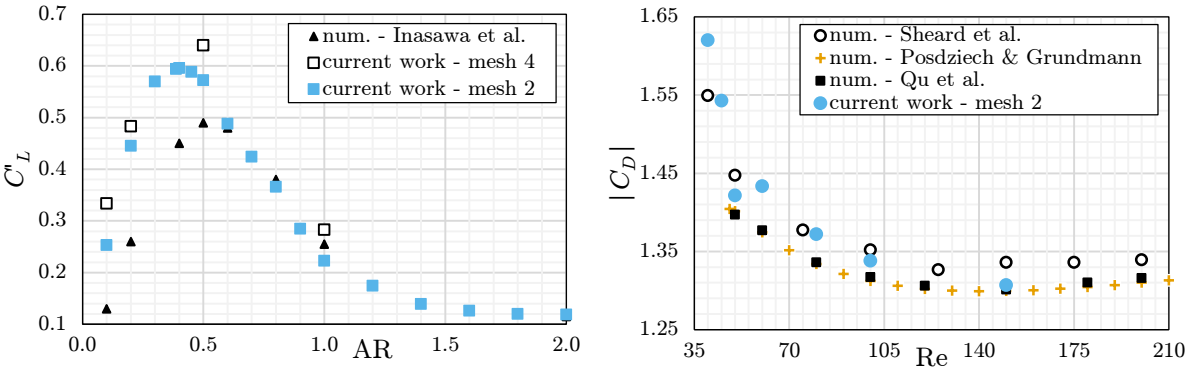

Figure 6: Comparison with literature of the fluctuating lift of a rectangle at different lengths (left) and of the mean drag of circular section at different Reynolds numbers (right).

A positive offset between current results and literature tendency is present in almost all points, at both graphs, and so it is for the Strouhal number and the drag fluctuation (not shown here). The elevated levels are a result of the choices made in the previous sections, where a shorter and coarser mesh would result in higher aerodynamic quantities. Although the limited precision for individual cases characterization, the trends are maintained and there is a global good fit when confronted to literature data.

In summary, considering the performed study and settings, all the results presented here are acknowledgedly slightly over estimated, at the order of 1 to 5%. However, even with the limited accuracy that is obtained, these small oscillations are negligible when confronted to the elevated differences that are searched in an optimization routine. Once the trends are shown to be respected, the use of the proposed numerical setup is considered adapted to the current application where the results are basically going to be compared

with each other.

3. Optimization framework

Once the numerical apparatus is well settled, the optimization algorithm is implemented. As the cost function is relatively expensive, care with the choice of the technique and its settings and the geometry parametrization is taken. Details of those two steps are presented next.

3.1. Optimization method

3.1.1. Particle Swarm optimization

Optimization is performed using the stochastic Particle Swarm Optimization (PSO) method, introduced by Kennedy and Eberhart [43]. It is based on the social behaviour of individuals. At each iteration T, the positions of the current best results for the objective/cost function at the individual (p_i) and swarm (g_i) levels are used as targets, along with the previous iteration velocity ($v_{i,T}$). The corresponding vectors from current location ($x_{i,T}$) in the design space are weighted and summed to give the following position ($x_{i,T+1}$). The location of the best values are updated and the process continues until swarm convergence. The considered ratios of each contribution (individual best, global best and last velocity) are regulated by cognitive (c_1), social (c_2) and inertial (c_w) factors, respectively. For the first 2 components, at every iteration and direction, independent and uniformly distributed between [0,1] random factors r_1 and r_2 are used. The later's role is to avoid convergence to local minima and to push the algorithm for further investigation of the design space.

$$x_{i,T+1} = x_{i,T} + c_w v_{i,T} + c_1 r_1 (p_i - x_{i,T}) + c_2 r_2 (g_i - x_{i,T}) \tag{4}$$

The g_{best} topology is used, what means that all particles communicate with the swarm from the beginning to the end of the optimization. It is a rather robust configuration, but less adapted in the case of several local minima. Particles that leave the design space are simply repositioned to the optimization domain edge, with no modification in its velocity. More strategies concerning the use of PSO are reported in [44].

3.1.2. Settings of the PSO

Preliminary tests were performed to select the optimization parameters for a similar test case ([33], symmetrical bluff body composed by 4 Bézier curves). Based on discrete 2D response surfaces and canonical benchmark functions in low dimension (Michalewicz in 2D and 3D), the values of $c_w = 0.6$ and $c_1 = c_2 = 1.2$ are selected for their good success rate at lower number of iterations/function evaluations. Although they vary slightly from the reported best on the literature [45, 44], the selected values were more adapted for the projected response function at a low dimension.

Similar analysis were performed with the number of elements in the swarm: for a compromise between the calculation time, that is the number of iterations, and the intended calculation precision, 36 particles are used for each optimization run (independently of the number of dimensions of the design space). Starting positions are either equally distributed points in the design space (grid of $3 \times 3 \times 2 \times 2$) or randomly distributed using Latin Hypercube Sampling (for 5 degrees of freedom and re-runs).

Maximum number of iterations is fixed at 30, value also based in previous empirical testing, and optimization stops when swarm stagnation is achieved. The selected criteria for stagnation is the average distance of the particles, quantified by the sum of the Euclidean distances of an arbitrary particle to the other members of the swarm divided by the number of particles; calculation is halted if this value is smaller than 0.001.

3.1.3. Other settings and implementation details

Although the response surface is not discrete, limitations regarding the element size constraint the results as noted in section 2.2.2. According to previous tests, geometrical resolution is at the order of $0.001d$, what traduces to the fact that for of any parameter, variations smaller than 0.001 will not result in a different solid domain. Consequently, to avoid unnecessary simulations, at the time the solver is called, the values of the geometrical parameters are rounded to the third decimal. In the case of recurrent calls to a previously simulated configuration, the former result is reused in the optimization routine.

Though convergence of aerodynamic quantities in time are measured in real-time for each simulation, it was observed that the behaviour is errant when different geometries are compared, leading to premature or retarded simulations stops when convergence criteria is used. To avoid an excessive number of idle processors in the optimization run, rather than defining a stop criteria, the number of flow cycles is constant for all cases and sufficient for a good convergence ($t = 360 \times d/U_\infty$, up to 50 lift cycles). According to the convergence curve presented in Figure 5, obtained precision of time solution is at order of 0.010%.

The optimization is performed in a cluster where each flow simulation is single cored, and for every iteration, the n agents are evaluated simultaneously. The optimizer environment is coded on Python, and the parallelism is done with the MPI standard using the mpi4py package [46]. Every iteration takes about 3 hours to be completed, and an average of 96 hours is necessary when the maximum number of iterations are performed.

3.2. Parametrized geometry

Final component of the shape optimization routine is the geometry. A low order parametric approach is employed, where a fine control of geometrical characteristics is not possible. This choice is coherent both with the chosen optimizer and to the fact that small nuances of the geometry are not relevant for the final

flow equilibrium for the regime in study, as presented in Section 2.2. In that sense, consequential shape modifications are expected in the search of geometries that present extreme aeroacoustic quantities.

The test geometry is a polygonal section, defined by 4 control points positioned in the edges of a circumscribing rectangle. With respect to the parametrisation used in [33], we aim at enlarging the varieties of aeroacoustic answers, here enabling non-zero mean lift and a simpler flow dynamics by fixing detachment at edges.

The dimensional parameters are the height d and the aspect ratio $AR = L/d$; four non-dimensional parameters, each in [0,1], define the distance of a control point from the origin of its containing edge in the outer rectangle, always in the axis direction: upstream edge ratio (k_u), downstream edge ratio (k_d), top edge ratio (k_t) and bottom edge ratio (k_b), as illustrated in 7, and define a point in the design space $P_4 = (k_u,k_d,k_t,k_b)$ for a selected rectangle (d, AR). Different combinations of those 4 parameters produce triangles, rectangles, lozenges or any other polygonal section with 4 edges. Once the height is fixed for constant blockage ratio, optimizations are performed up-to 5 dimensions.

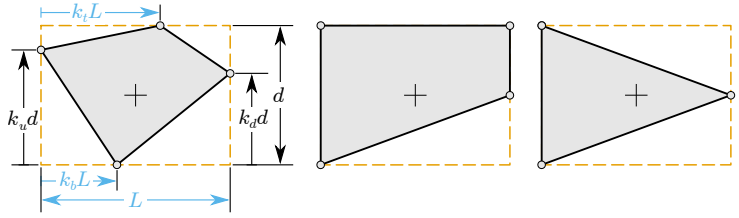

Figure 7: Scheme of the parametrized geometry (left) and examples of the possible geometries: P_4 = (1.0, 0.5, 1.0, 0.0), center, and P_4 = (0.0, 0.5, 0.0, 0.0), right.

Due to the nature of the parametrization, there are at least two points in the design space that produce the same geometry when shape is mirrored in y_1 axis, and would produce the same aeroacoustical outcome, only with reverse mean lift, for example, P_4 = (0.5; 0.3; 0.2; 0.0) and P_4 = (0.5; 0.7; 0.0; 0.2). This property generates at least 2 local minima, but once they represent the same geometry and bulk quantities (a single globally best geometry) this is not accounted in the conception of the optimization routine. The effects of having such characteristic in the response surface is not checked and there is no inspection step to avoid that such duplicates are evaluated twice.

4. Optimization results

For investigating the mechanisms associated with an aeolian tone, both extreme shapes are of interest. That is why the optimization routine was employed for minimization and maximization (minimizing the inverse). In addition to the optimization of W, that of the fluctuating lift C'_L is performed as it is identified as the key ingredient for bluff body noise. Optimization for the mean drag $|C_D|$ is also considered, in order

to check if the present optimizer is able to return consistent output with respect to steady aerodynamics, which are better known than aeroacoustics. The results are presented here, starting by a description of the optimal shapes and the corresponding aerodynamic and acoustic coefficients, followed by the analysis of the physics that drive noise reduction or amplification. The optimization process behaviour is discussed subsequently.

4.1. Optimal shapes and coefficients

Pairs of optimal shapes and their corresponding aerodynamic quantities are listed in Table 3, where the cost/objective values are in bold; the normalized acoustic power, $W_a = W/(d\rho_0 U_\infty^3)$, is presented. Obtained values for rectangles of different aspect ratios are also tabulated and serve as a reference for comparison with the optimal sections. Graphical representation of the obtained shapes is available in Figure 8.

Table 3: optimization outputs. On each line, the optimized quantity is in bold font. On the lower part of the table, the data for flows over rectangles are given for comparison (due to the symmetry, mean lift is null, so omitted from the rectangle lines).

objective	AR	k_u	k_d	k_t	k_b	$\lvert C_L\rvert$	$\lvert C_D\rvert$	C'_L	C'_D	St	$W_a, 10^{-5}$
min $\lvert C_D\rvert$ *	1.000	0.113	1.000	0.000	1.000	0.153	**1.274**	0.220	0.017	0.180	1.72
max $\lvert C_D\rvert$ *	1.000	0.946	0.000	0.000	0.882	1.614	**2.259**	0.458	0.127	0.181	8.60
min C'_L *	1.000	0.935	0.000	1.000	0.000	-0.038	1.288	**0.210**	0.013	0.174	1.52
max C'_L *	1.000	1.000	0.275	0.000	0.242	0.391	2.258	**1.058**	0.201	0.171	40.17
min W_a *	1.000	0.959	0.000	1.000	0.000	-0.005	1.311	0.211	0.010	0.171	**1.50**
max W_a *	1.000	1.000	0.285	0.000	0.201	0.330	2.233	1.055	0.195	0.172	**40.22**
min W_a $^+$	2.000	1.000	0.111	0.956	0.000	-0.062	1.127	0.101	0.002	0.165	**0.33**
max W_a $^+$	1.100	1.000	0.279	0.000	0.234	0.331	2.117	1.066	0.186	0.164	**38.79**
rectangle	0.500	1	0	1	0	-	1.895	0.572	0.077	0.193	12.83
square	1.000	1	0	1	0	-	1.347	0.223	0.011	0.167	1.63
rectangle	2.000	1	0	1	0	-	1.138	0.119	0.002	0.164	0.45

*: fixed AR; $^+$: AR as a parameter in the optimization, $AR \in [0.5, 2.0]$.

4.1.1. Mean drag at $AR = 1.0$

Although the viscosity effects are not negligible for the selected flow conditions (Sheard at al. [40] presented that 21% of the drag was from the viscous shear tensor for a square cylinder at the same regime), pressure forces remain the major component of the drag. From a preliminary analysis, the obtained velocity

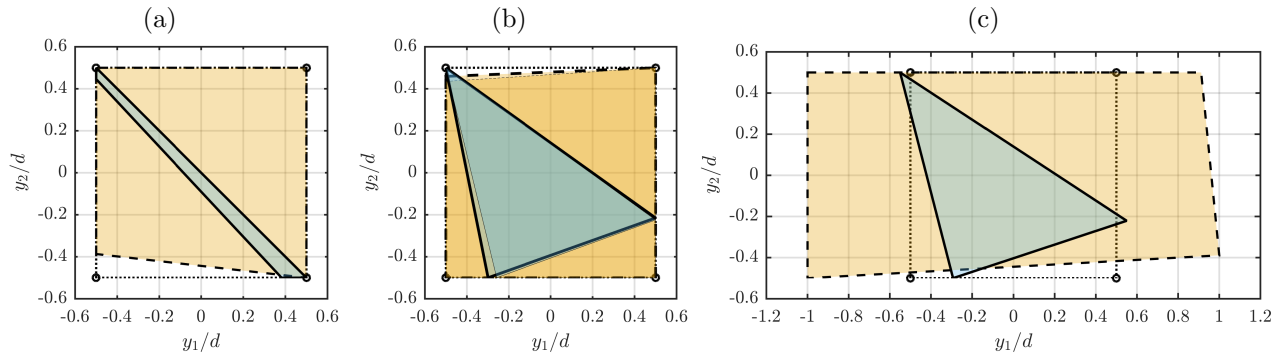

Figure 8: Optimal shapes. Dotted line is the square. (a) minimum $|C_D|$ (dashed line) and maximum $|C_D|$ (solid line) at fixed AR = 1.0; (b) minimum C'_L (thick dashed line) and W (thin dashed line) and maximum C'_L (thick solid line) and W (thin solid line) at fixed AR= 1.0; (c) minimum W (thick dashed line) and maximum W (thick solid line) for variable AR$\in [0.5, 2.0]$ (5D optimization).

fields do not vary much, thus viscous efforts are not discussed here. The mean pressure field for the optimal pair and the square are illustrated in Figure 9.

The biggest drag amounts to about 1.7 that of the square shape and is encountered for a flat plate like geometry (Figure 8a). The changes in the level of suction are small, however, the modification in the disposition of the vortex in the wake created an important depression zone downstream of the section that overcomes the reduction of the pressure on the upstream face (Figure 9c) due to detachment. It is known that the drag only increases with the angle of attack of a plate. At this fixed aspect ratio, this is the biggest angle possible.

The minimum drag geometry, Figure 8a, is a slightly distorted square, with the bottom edge elevated at the upstream portion. The resulting flow, Figure 9a, is slightly asymmetrical, and when compared to the square the mean drag is reduced by 5.4%. There is a decrease in the surface submitted to the dynamic head, and since the bottom edge normal has a component in the streamwise direction, the suction on this edge also contributes to drag reduction.

4.1.2. Lift fluctuation and acoustic power

Minimum/maximum RMS lift and acoustic power are searched independently at $AR = 1$. As noted on their geometrical parameters and aerodynamic results in Table 3, the obtained geometries are quite similar (a few % on geometrical parameters, even lower for flow quantities), see Figure 8b, and differences may be considered within the uncertainty of the calculations. Although the answers are virtually identical, it is noted that the RMS lift is still better when it is the objective function than when the latter is the acoustic power, and vice-versa, and this constitutes a sign of the robustness of the optimization procedures.

Similarly to the minimum drag geometry, the minimum W is associated with a deformed square. For this case, the upper edge is lowered at the upstream portion, close to a mirrored version of the previous

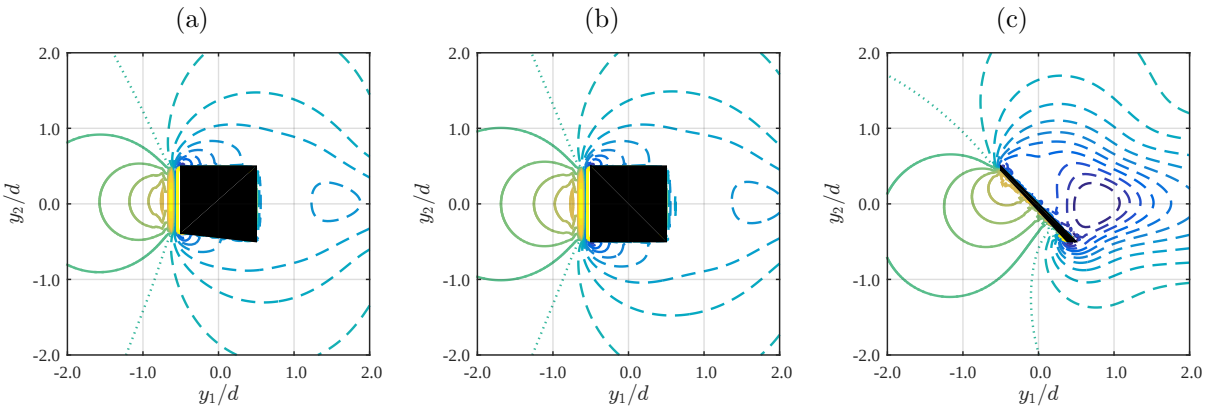

Figure 9: Mean pressure field for (a) the minimum drag shape, (b) the square and (c) the maximum drag shape. Pressure coefficient contour, interval of 0.1. Continuous line for positive, dashed line for negative and dotted line for null.

case. The obtained answer is only 0.4 dB quieter than the square, and is likely to be associated with a small increase of viscous dissipation on the top of the obstacle provoked by the enlargement of the wall, what reflects in slightly weaker vortex. The geometry that amplifies the noise power is a back-pointing triangle, consistently with the result obtained for a parameterization of the geometry based on Bezier's curves [33] and with a parametric study on canonical shapes [47]. Here, it radiates 25 times (14 dB) more power than the square section.

Optimizations of the acoustic power at 5 degrees of freedom (DoF) are also performed, for $0.5 \leq AR \leq 2.0$, and the obtained shapes are illustrated in Figure 8c. As for the previous cases, a deformed rectangle is obtained for minimum W, for the longest geometry possible. In this case, the deviation is on the other sense, at the downstream portion of the bottom edge. The maximum noise is obtained with another triangle, but not in the minimum aspect ratio. There is no strong increase with respect to the fixed AR optimization (see discussion in Section 4.3.2) while lengthening the shape from $AR = 1$ to $AR = 2$ reduces the noise by 5.6 dB, the rectangle still being close ($\approx$ 1dB) to the optimal.

As a conclusion, globally, even for a very limited set of tested geometries at a fixed blockage, a ratio of 1.8 for the mean drag and 20 dB for the noise is observed between the extrema of the present study.

4.2. Physics and optimization paths for the acoustic power

In this section, the effect of shape on acoustic power is discussed, based on the optimization results. The driving geometrical parameters are first extracted, before the flow characteristics that are associated with a modification of noise emission are analyzed. Finally, the seeming link between mean drag and lift fluctuations is objectivized.

4.2.1. Shape

At given aspect ratio, modifications of the upper and lower edges are the most active in terms of the aerodynamic and aeroacoustic answers, which corresponds to profiling or anti-profiling the geometry, rather than sophisticating its front or back side. From the observation of vorticity fields of the shape with minimal noise and the rectangular section of $AR = 2.0$ (not shown), it is believed that, at that length, the small modifications in the lateral edge's angle are close to insignificant when compared to the effect of the length itself and further investigation of that influence is performed.

Figure 10 shows the obtained acoustic power for all the points evaluated in the 2 optimization runs with aspect ratio as a parameter. Even if such plot may not represent fairly each region of the parameter space, it reproduces globally the evolution noticed for a given geometry, such as the rectangle and the back-pointing triangle: as investigated specifically in [47], the lift fluctuation increases for low AR, due to the increase of available surface for lift generation; after a maximum is reached, the lift fluctuation decreases due to a global reduction of flow unsteadiness, that is, there is less pressure fluctuations on the lateral surfaces for more elongated bodies. This evolution, described by Inasawa et al. [42] for rectangles, is found universal, however the lift fluctuation maximum and the AR at which it is reached, are specific for each cross section: this AR is around 0.4 for the rectangle and around 1.1 for the back-pointing triangle. It is also noted in [47] that this AR leads to a maximum for the Strouhal number too. However, for the triangle, the drag fluctuation undergoes a strong decrease for $0.5 \leq AR \leq 1.5$, resulting in a maximum acoustic power rather at $AR \approx 0.9$, as visible in Figure 10. Back to the optimization problem, the modification of the aspect ratio affects the frequency of the wake, thus contributing to a larger discrimination between the minimum and the maximum noise than what was obtained at fixed AR.

Figure 10 also shows how close the rectangle and the back-pointing triangle are to the optimal section, for the acoustic power minimization and maximization respectively. Anticipating the next section, the main difference between these two canonical shapes is that the triangle generates stronger interactions of the shear layers, which imprint the wall with a bigger C'_L and consequently result in higher acoustic power. This is aligned with the canonical experiment using a splitter plate by Roshko [48] and its repercussions: the splitter plate lengthens the shape and pushes the shear layer interaction area downstream of the lifting surface. For a back-pointing triangle, the interaction starts before the trailing edge and with stronger vortices.

4.2.2. Flow quantities

Vorticity snapshots for both minimum and maximum noise flows at $AR = 1$ are presented in Figure 11. The field for the flow over the square section is also plotted for comparison. Considering that one of them is associated with 25 times more acoustic radiation than the two others, it is striking that the vorticity fields in the wake do not exhibit such a huge difference. Note in Figure 11c that the vortex street of the noisy flow remains symmetrical, but the symmetry axis is angled towards the upper boundary. This may change the directivity of the sound, but the evaluation of this aspect of the acoustical field is not available from the

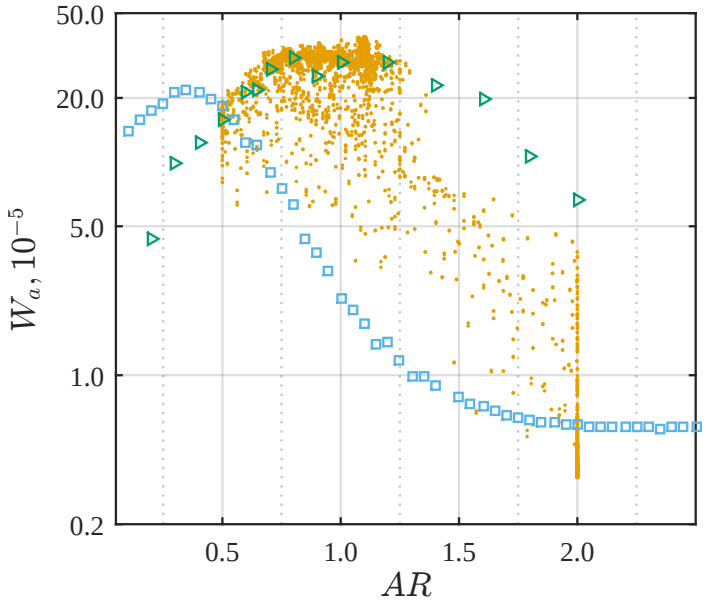

Figure 10: Acoustic power as a function of the body length: dots include all the geometries evaluated for the 5 DoF optimizations, square and triangle markers are for rectangles and back-pointing triangles, respectively.

tools used in this work and does not change the total acoustic power.

The similarity of the optimal shapes for lift fluctuation and acoustic power (see Figure 8b) corroborates with the fact that the transverse fluctuations of the flow, incorporated in the fluctuating lift, are the most important element in the description of the tonal noise of 2D bluff bodies [47]. Indeed, based on the acoustic model (1), remaining variables are the Mach number, the fluctuating drag, and the Strouhal number number. The compressibility effects (M) are unchanged between the geometries due the incompressible source assumption and fixed flow conditions. For C'_D, it remains one order lower than the fluctuating lift. Interestingly, when comparing the minimum and the maximum, the increase of C'_D reaches nearly a factor 100 (see Table 3). That means that even if the drag contribution to the noise remains small, it has a wider range and thus can be more affected by shape modifications. Recall, moreover, that oscillating at twice the lift frequency, its effect on time average acoustic power is doubled. As for St, Table 3 shows that there is a really small variation of its value, between 0.164 and 0.180 (this corresponds to $\pm 10\%$ around the median). This is due to a fixed body height (and somehow limited other geometry modifications), which strongly constrains the wake width, the latter being the main driver of the wake frequency [49].

As introduced before and quantitatively discussed in [47], the interaction of both mixing layers is increased for the noisy flow, what results in shorter recirculation and vortex formation lengths, and simultaneously stronger vortex, as presented in Figure 11. The interaction of those structures with the walls of the obstacle

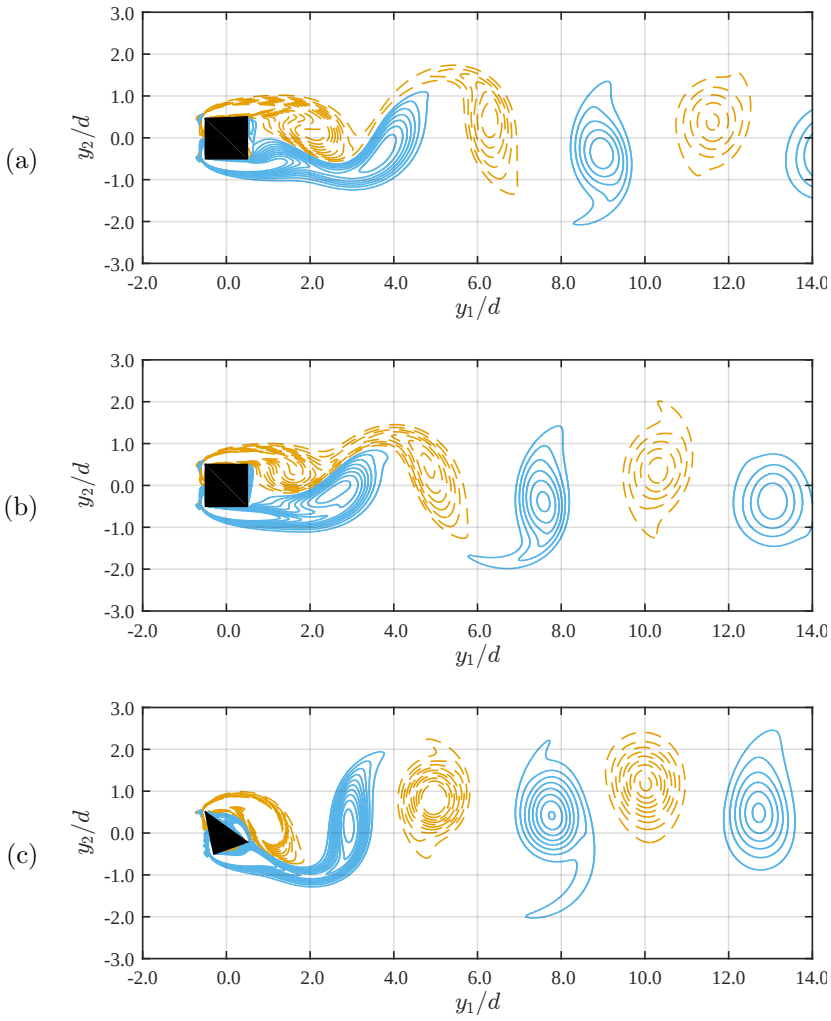

Figure 11: Snapshots of vorticity contours for (a) minimum acoustic power shape, (b) a square and (c) maximum acoustic power shape, for AR = 1. Interval of 0.3 U_∞/d. Continuous line for positive and dashed line for negative values.

causes larger C'_D and C'_L.

4.2.3. Link between mean drag and lift fluctuations

A closer look at Table 3 shows that even when it is not the objective, the mean drag is strongly increased between the minimum and the maximum. Moreover, for rectangular section, increasing the aspect ratio reduces both the mean drag and the lift fluctuation. This suggests that both quantities could be correlated [50]. A statistical relationship between them has been educed in a recent contribution [47]. Here, the correlation is visualized by plotting the quantities on the two axis of the same graph in Figure 12 for all the flow cases simulated for all the optimization runs of the present study (about 17000 geometries). Despite the dispersion of the data, a global common trend is noteworthy. The values for the rectangular and back-pointing triangular sections follow well the mainstream.

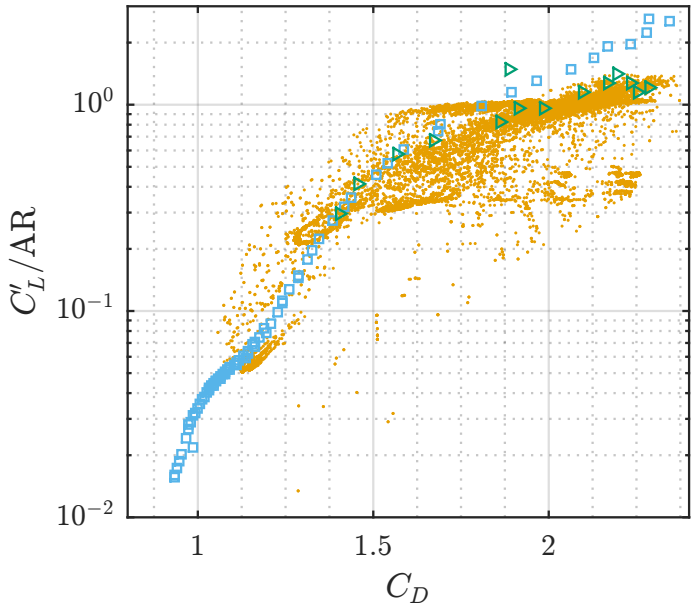

Figure 12: Lift fluctuation normalised by lifting surface for different geometries *versus* mean drag: dots include all the geometries evaluated for all the present optimization runs, square and triangle markers are for rectangles and back-pointing triangles, respectively.

Note that the lift fluctuation is normalized by the breadth of the body (AR), yielding rather the average pressure fluctuation on the available solid surface. Indeed, even if the physical reason of such correlation deserves further investigation, it is likely the result of a common cause, which is believed to be the strength of the low-pressure vortices of opposite sign [18]: during their generation at each side of the body and their shedding in the wake, they induce mean base pressure and wall pressure fluctuation on the lifting surfaces at the same time.

Another interesting comportment that outlays with the associations of mean drag and fluctuating lift, is that, when one of them is aimed, the other may not be the optimal at the end of the optimization. Setting the square as reference, when aiming for minimum noise there is a reduction of 2.7% of the drag. Oppositely, when searching for minimum drag, there is a 0.23 dB increase of acoustical noise. Although this conclusion is limited to the regime and the characteristics of the test geometry, this may be a rather untoward trend, since the aeroacoustics is most commonly neglected in face of the drag, that touches directly the aerodynamic performance. Nevertheless, this is a minor drawback balanced by the huge advantage of predicting aeroacoustics from only mean flow properties that the abovementionned correlation between mean drag and lift fluctuation could allow.

4.3. Behavior of the optimization process

4.3.1. Feedback on shape parameters and IBM

As can be seen on the obtained geometrical parameters (Table 3), at least 2 of the 4 edge ratios were always on the limits of the design space (either 0 or 1). It is observed that, after a few iterations, these final values are already selected and the search is reduced to a 3D or 2D design space. In terms of the optimization procedure, the search for the best response is facilitated, however, it shows that the choice of the parametrization may be poor, since only a part of the variables retain the control of the cost function.

For the maximum mean drag shape, the result is doubted due to the reduced number of solid points, with some horizontal slices (in the streamwise direction) of the body having only one solid element. This is physically questionable given the IBM resolution and the spatial derivation stencil. To check the consistency of the solution, the simulation was re-run with mesh 4, where slices with single or double solid elements only exist at the extreme upper part of the discrete shape. There are no significant changes in the flow, but small variations in the aerodynamic quantities are obtained: -2.6% of mean lift, -9.4% of mean drag, +0.9% of RMS lift and + 21.9% of RMS drag and -0.7% of St. However, specially for the aimed quantity ($|C_D|$), the original values are of the same order and consistently higher than the minimum, giving another hint that the optimization result and the numerical setup are reliable.

4.3.2. Local vs. global extrema

Besides the use of PSO, a technique already more adapted to complex response function than gradient based optimizers, there are no extra efforts to mitigate the chances to converge in local minima, such as more restraining topologies. For some optimizations performed for this study, there were clear indications that the obtained geometries were not the global minimum, either from the attained value or from the related form. In those cases, the optimization was relaunched from the beginning and the final value was compared to the previous answer and only the best (the values that are considered global minima or maxima) are presented.

For instance, as can be seen on Table 3, the maximum noise obtained for the 5 DoF optimization ($W_a = 38.79 \times 10^{-5}$) is lower than the value obtained at fixed length ($W_a = 40.22 \times 10^{-5}$). The same configuration was thus optimized 3 times, starting for a design space of $AR \in [0.5; 2.0]$ for the aspect ratio for the first two runs and [0.75; 1.25] for the final one, and even so the final result is clearly not the global maximum, being smaller than the maximum at fixed AR. The obtained misbehaviour contributes to the conclusion that, for every geometry (associated to a specific P_4 coordinates point), there is a unique length that maximizes the noise (see Section 4.2.1), in such a way that there are multiple local maxima in the design space. Besides the use of a different swarm topology, a re-setting of the number of particles, total number of iterations and the optimization coefficients could help the swarm to reach the global optimum.

5. Conclusions

An optimization routine based on a stochastic technique is presented for the tonal noise of a compact source. The geometry is an infinite span cylinder with a polygonal section modelled by an IBM approach; the acoustics is calculated by a single formula model issued from Curle's analogy, with sources obtained from the results of an incompressible aerodynamic solver at $\mathrm{Re} = 150$.

The feasibility of the performed optimization procedure relays fundamentally on the robustness of both the optimizer (PSO) and the IBM. In that way, the management of the tested geometries was possible without direct interference after both optimization and flow simulation settings were defined in careful preliminary studies. Simultaneously, the use of an acoustic model that is able of analytically returns the acoustic power from global flow statistics was an essential component of the proposed framework.

Such shape optimization for aeroacoustics in the laminar regime was partly designed in order to emphasize the phenomena, thus guiding intuition for a more relevant analysis [47] of the influence of shape on noise source mechanisms. From the obtained optima, it is clear that the key to reduce the noise production is to decrease the strength and the interaction between the top and bottom shear layers in the wake of a bluff body, such that long or bluffer geometries, therefore, the ones where the interaction of the mixing layers is reduced, are the ones with smallest C'_L and consequently lower acoustic power. At fixed height and length, that reduction was obtained with small increase of one of the lateral edges of the geometry and thus increase viscous dissipation of the forming vortex. From tests with a modifiable length, the aspect ratio is concluded to be the most important factor for reducing the noise. On the other way, maximum acoustic power is associated with back-facing triangles, where the effect is inverted: more interaction between the layers and stronger vortex in the near-wake.

It is observed that, under the limitations of both the space discretization and the geometry complexity, modifications that increase or decrease the acoustic emission are mainly associated with modifying the RMS lift. Besides the known fact that it is the fundamental fuel for bluff body noise, the incapacity of the geometry to influence the whistling frequency at the same impact is an important conclusion regarding not only the acoustics, but potential applications on energy harvesting.

Acknowledgements

Computations have been performed on the supercomputer facilities of the Mésocentre de Calcul de Poitou- Charentes. The PhD funding of the main author of this work was provided by the Ministère de l'Enseignement Supérieur et de la Recherche (MESR, french Ministry of Higher Education and Research), which is greatly appreciated. The authors are also grateful to Laurent Cordier for fruitful discussions concerning optimization strategies in fluid flow.

References

[1] F. Margnat, V. Ioannou, S. Laizet, A diagnostic tool for jet noise using a line-source approach and implicit large-eddy simulation data, Comptes Rendus Mécanique 346 (10) (2018) 903 – 918. doi:https://doi.org/10.1016/j.crme.2018.07.007.
URL http://www.sciencedirect.com/science/article/pii/S1631072118301530

[2] J. E. F. Williams, D. L. Hawkings, M. J. Lighthill, Sound generation by turbulence and surfaces in arbitrary motion, Philosophical Transactions of the Royal Society of London. Series A, Mathematical and Physical Sciences 264 (1151) (1969) 321–342. arXiv:https://royalsocietypublishing.org/doi/pdf/10.1098/rsta.1969.0031, doi:10.1098/rsta.1969.0031.
URL https://royalsocietypublishing.org/doi/abs/10.1098/rsta.1969.0031

[3] N. Curle, The influence of solid boundaries upon aerodynamic sound, Proceedings of the Royal Society of London A: Mathematical, Physical and Engineering Sciences 231 (1187) (1955) 505–514. arXiv:http://rspa.royalsocietypublishing.org/content/231/1187/505.full.pdf, doi:10.1098/rspa.1955.0191.
URL http://rspa.royalsocietypublishing.org/content/231/1187/505

[4] M. J. Lighthill, On sound generated aerodynamically. I. general theory, Proc. Roy. Soc. A 223 (1952) 1–32.

[5] A. Powell, Theory of vortex sound, The Journal of the Acoustical Society of America 36 (1) (1964) 177–195. arXiv:https://doi.org/10.1121/1.1918931, doi:10.1121/1.1918931.
URL https://doi.org/10.1121/1.1918931

[6] M. S. Howe, Theory of Vortex Sound, 2002.

[7] J. E. F. Williams, L. H. Hall, Aerodynamic sound generation by turbulent flow in the vicinity of a scattering half plane, Journal of Fluid Mechanics 40 (4) (1970) 657–670. doi:10.1017/S0022112070000368.

[8] D. Crighton, Basic principles of aerodynamic noise generation, Progress in Aerospace Sciences 16 (1) (1975) 31 – 96. doi:https://doi.org/10.1016/0376-0421(75)90010-X.
URL http://www.sciencedirect.com/science/article/pii/037604217590010X

[9] X. Gloerfelt, F. Pérot, C. Bailly, D. Juvé, Flow-induced cylinder noise formulated as a diffraction problem for low Mach numbers, J. Sound Vib. 287 (2005) 129–151.

[10] S. Piantanida, V. Jaunet, J. Huber, W. R. Wolf, P. Jordan, A. V. G. Cavalieri, Scattering of turbulent-jet wavepackets by a swept trailing edge, The Journal of the Acoustical Society of America 140 (6) (2016) 4350–4359. arXiv:https://doi.org/10.1121/1.4971425, doi:10.1121/1.4971425.
URL https://doi.org/10.1121/1.4971425

[11] A. Powell, Aerodynamic noise and the plane boundary, The Journal of the Acoustical Society of America 32 (8) (1960) 982–990. arXiv:https://doi.org/10.1121/1.1908347, doi:10.1121/1.1908347.
URL https://doi.org/10.1121/1.1908347

[12] X. Gloerfelt, F. Margnat, Effect of Mach number on boundary layer noise, in: 20th AIAA/CEAS Aeroacoustics Conference, AIAA Paper 2014-3291, Atlanta, GA, 2014. arXiv:https://arc.aiaa.org/doi/pdf/10.2514/6.2014-3291, doi:10.2514/6.2014-3291.
URL https://arc.aiaa.org/doi/abs/10.2514/6.2014-3291

[13] M. J. Lighthill, The bakerian lecture, 1961 sound generated aerodynamically, Proceedings of the Royal Society of London. Series A. Mathematical and Physical Sciences 267 (1329) (1962) 147–182. doi:10.1098/rspa.1962.0090.
URL https://royalsocietypublishing.org/doi/abs/10.1098/rspa.1962.0090

[14] C. Moser, E. Lamballais, F. Margnat, V. Fortuné, Y. Gervais, Numerical study of Mach number and thermal effects on sound radiation by a mixing layer, Int. J. Aeroacoutics 11 (5-6) (2012) 555–580.

[15] O. M. Phillips, The intensity of aeolian tones, Journal of Fluid Mechanics 1 (6) (1956) 607–624. doi:10.1017/S0022112056000408.

[16] M. S. Howe, Cambridge monographs on mechanics, in: C. U. Press (Ed.), Acoustics of fluid-structure interactions, 1998, pp. 157–166.

[17] Keefe, An investigation of the fluctuating forces acting on a stationary circular cylinder in a subsonic stream and of the associated soud field (utia report no. 76), Tech. rep., Institute of Aerophysics, University of Toronto (UTIA) (1961).

[18] A. Roshko, Perspectives on bluff body aerodynamics, Journal of Wind Engineering and Industrial Aerodynamics 49 (1) (1993) 79 – 100. doi:https://doi.org/10.1016/0167-6105(93)90007-B.
URL http://www.sciencedirect.com/science/article/pii/016761059390007B

[19] F. Margnat, Hybrid prediction of the aerodynamic noise radiated by a rectangular cylinder at incidence, Computers and Fluids 109 (4) (2015) 13–26.

[20] D. E. Goldberg, Genetic Algorithms in Search, Optimization and Machine Learning, 1st Edition, Addison-Wesley Longman Publishing Co., Inc., Boston, MA, USA, 1989.

[21] R. Storn, K. Price, Differential evolution – a simple and efficient heuristic for global optimization over continuous spaces, Journal of Global Optimization 11 (4) (1997) 341–359. doi:10.1023/A:1008202821328.
URL http://dx.doi.org/10.1023/A:1008202821328

[22] M. Dorigo, V. Maniezzo, A. Colorni, Ant system: Optimization by a colony of cooperating agents, Trans. Sys. Man Cyber. Part B 26 (1) (1996) 29–41. doi:10.1109/3477.484436.
URL http://dx.doi.org/10.1109/3477.484436

[23] J. Kennedy, R. Eberhart, Particle swarm optimization, in: Neural Networks, 1995. Proceedings., IEEE International Conference on, Vol. 4, 1995, pp. 1942–1948 vol.4. doi:10.1109/ICNN.1995.488968.

[24] S. Krajnovic, Shape optimization of high-speed trains for improved aerodynamic performance, in: Proceedings of the Institution of Mechanical Engineers, Part F: Journal of Rail and Rapid Transit, 2009, pp. 439–452.

[25] C. Praveen, R. Duvigneau, Low cost pso using metamodels and inexact pre-evaluation: Application to aerodynamic shape design, Computer Methods in Applied Mechanics and Engineering 198 (9) (2009) 1087 – 1096. doi:https://doi.org/10.1016/j.cma.2008.11.019.
URL http://www.sciencedirect.com/science/article/pii/S0045782508004155

[26] S. Beigmoradi, H. Hajabdollahi, A. Ramezani, Multi-objective aero acoustic optimization of rear end in a simplified car model by using hybrid robust parameter design, artificial neural networks and genetic algorithm methods, Computers & Fluids 90 (Supplement C) (2014) 123 – 132. doi:https://doi.org/10.1016/j.compfluid.2013.11.026.
URL http://www.sciencedirect.com/science/article/pii/S0045793013004659

[27] S. B. Yao, D. L. Guo, Z. X. Sun, D. W. Chen, G. W. Yang, Parametric design and optimization of high speed train nose, Optimization and Engineering 17 (3) (2016) 605–630. doi:10.1007/s11081-015-9298-6.
URL http://dx.doi.org/10.1007/s11081-015-9298-6

[28] K. Karthik, M. Vishnu, S. Vengadesan, S. Bhattacharyya, Optimization of bluff bodies for aerodynamic drag and sound reduction using cfd analysis, Journal of Wind Engineering and Industrial Aerodynamics 174 (2018) 133 – 140. doi:https://doi.org/10.1016/j.jweia.2017.12.029.
URL http://www.sciencedirect.com/science/article/pii/S016761051730911X

[29] S. Becker, C. Hahn, M. Kaltenbacher, R. Lerch, Flow-induced sound of wall-mounted cylinders with different geometries, AIAA Journal 46 (9) (2008) 2265–2281. doi:10.2514/1.34865.
URL https://doi.org/10.2514/1.34865

[30] W. F. King, E. Pfizenmaier, An experimental study of sound generated by flows around cylinders of different cross-section, Journal of Sound and Vibration 328 (3) (2009) 318–337.
URL http://www.sciencedirect.com/science/article/pii/S0022460X09006221

[31] Y. Oguma, T. Yamagata, N. Fujisawa, Measurement of sound source distribution around a circular cylinder in a uniform

flow by combined particle image velocimetry and microphone technique, Journal of Wind Engineering and Industrial Aerodynamics 118 (2013) 1 – 11. doi:https://doi.org/10.1016/j.jweia.2013.04.003.
URL http://www.sciencedirect.com/science/article/pii/S0167610513000743

[32] W. J. G. S. Pinto, F. Margnat, Y. Gervais, Effect of cross-section on flow three-dimensionality for prismatic bodies and the associated noise emission, in: 25th AIAA/CEAS Aeroacoustics Conference (Aeroacoustics 2019), AIAA Paper 2019-2531, Delft, The Netherlands, 2019.

[33] W. J. G. da Silva Pinto, F. Margnat, A shape optimization procedure for cylinders aeolian tone, Computers and Fluids 182 (2019) 37 – 51. doi:https://doi.org/10.1016/j.compfluid.2019.02.002.
URL http://www.sciencedirect.com/science/article/pii/S0045793019300283

[34] S. Laizet, E. Lamballais, High-order compact schemes for incompressible flows: A simple and efficient method with quasi-spectral accuracy, J. Comp. Phys. 228 (2009) 5989–6015.

[35] F. Margnat, X. Gloerfelt, On compressibility assumptions in aeroacoustic integrals: a numerical study with subsonic mixing layers, Journal of the Acoustical Society of America 135 (2014) 3252–3263.

[36] D. Goldstein, R. Handler, L. Sirovich, Modeling a no-slip boundary condition with an external force field, J. Comp. Phys. 105 (1993) 354–366.

[37] F. Margnat, V. Morinière, Behavior of an immersed boundary method in unsteady flows over sharp-edged bodies, Computers and Fluids 38 (6) (2009) 1065–1079.

[38] A. Sohankar, C. Norberg, L. Davidson, Low-reynolds-number flow around a square cylinder at incidence: study of blockage, onset of vortex shedding and outlet boundary condition, International Journal for Numerical Methods in Fluids 26 (1) (1998) 39–56. doi:10.1002/(SICI)1097-0363(19980115)26:1<39::AID-FLD623>3.0.CO;2-P.
URL http://dx.doi.org/10.1002/(SICI)1097-0363(19980115)26:1<39::AID-FLD623>3.0.CO;2-P

[39] O. Posdziech, R. Grundmann, A systematic approach to the numerical calculation of fundamental quantities of the two-dimensional flow over a circular cylinder, Journal of Fluids and Structures 23 (3) (2007) 479 – 499. doi:https://doi.org/10.1016/j.jfluidstructs.2006.09.004.
URL http://www.sciencedirect.com/science/article/pii/S0889974606001083

[40] G. J. Sheard, K. Hourigan, M. C. Thompson, Computations of the drag coefficients for low-reynolds-number flow past rings, Journal of Fluid Mechanics 526 (2005) 257 – 275. doi:10.1017/S0022112004002836.

[41] L. Qu, C. Norberg, L. Davidson, S.-H. Peng, F. Wang, Quantitative numerical analysis of flow past a circular cylinder at reynolds number between 50 and 200, Journal of Fluids and Structures 39 (Supplement C) (2013) 347 – 370. doi:https://doi.org/10.1016/j.jfluidstructs.2013.02.007.
URL http://www.sciencedirect.com/science/article/pii/S0889974613000388

[42] A. Inasawa, M. Asai, T. Nakano, Sound generation in the flow behind a rectangular cylinder of various aspect ratios at low mach numbers, Computers & Fluids 82 (Supplement C) (2013) 148 – 157. doi:https://doi.org/10.1016/j.compfluid.2013.05.006.
URL http://www.sciencedirect.com/science/article/pii/S0045793013001928

[43] R. J. Kennedy, Eberhart, Particle swarm optimization, in: Proceedings of IEEE International Conference on Neural Networks IV, pages, Vol. 1000, 1995.

[44] R. Poli, J. Kennedy, T. Blackwell, Particle swarm optimization, Swarm Intelligence 1 (1) (2007) 33–57. doi:10.1007/s11721-007-0002-0.
URL https://doi.org/10.1007/s11721-007-0002-0

[45] I. C. Trelea, The particle swarm optimization algorithm: convergence analysis and parameter selection, Information Processing Letters 85 (6) (2003) 317 – 325. doi:https://doi.org/10.1016/S0020-0190(02)00447-7.
URL http://www.sciencedirect.com/science/article/pii/S0020019002004477

[46] L. Dalcín, R. Paz, M. Storti, J. D'Elía, Mpi for python: Performance improvements and mpi-2 extensions, Journal of Parallel and Distributed Computing 68 (5) (2008) 655 – 662. doi:https://doi.org/10.1016/j.jpdc.2007.09.005.
URL http://www.sciencedirect.com/science/article/pii/S0743731507001712

[47] W. J. G. S. Pinto, F. Margnat, Y. Gervais, Influence of cross-section on the aeolian tone: a numerical study in the laminar regime, in: 25th AIAA/CEAS Aeroacoustics Conference (Aeroacoustics 2019), 20-24 May, Delft, The Netherlands, 2019.

[48] A. Roshko, On the drag and shedding frequency of two-dimensional bluff bodies, Tech. rep., National Advisory Committee for Aeronautics (1954).

[49] A. Roshko, On the wake and drag of bluff bodies, Journal of the Aeronautical Sciences 22 (2) (1955) 124–132. doi:10.2514/8.3286.
URL https://doi.org/10.2514/8.3286

[50] J. D. Revell, R. A. Prydz, A. P. Hays, Experimental study of aerodynamic noise vs drag relationships for circular cylinders, AIAA Journal 16 (9) (1978) 889–897. arXiv:https://doi.org/10.2514/3.60982, doi:10.2514/3.60982.
URL https://doi.org/10.2514/3.60982